Interhemispheric Asymmetry of the Thermospheric Neutral Density Response to the 7–9 September 2017 Geomagnetic Storms

Zhu, Qingyu; Lu, Gang; Lei, Jiuhou; Deng, Yue; Doornbos, Eelco; van den IJssel, Jose; Siemes, Christian

DOI
10.1029/2023GL103208

Publication date
2023

Document Version
Final published version

Published in
Geophysical Research Letters

AGU ADVANCING EARTH AND SPACE SCIENCE

Geophysical Research Letters®

RESEARCH LETTER
10.1029/2023GL103208

Key Points:

- Thermosphere-ionosphere-electrodynamic general circulation model captures the observed interhemispheric asymmetry (IHA) in the neutral density response to the 7–9 September 2017 geomagnetic storms
- The IHA in the neutral density response results from the IHA in traveling atmospheric disturbances and mean molecular mass
- The observed IHA in the neutral density response is not caused by direct Joule heating dissipated at the same local time

Supporting Information:

Supporting Information may be found in the online version of this article.

Correspondence to:

Q. Zhu,
qingyu@ucar.edu

Citation:

Zhu, Q., Lu, G., Lei, J., Deng, Y., Doornbos, E., van den IJssel, J., & Siemes, C. (2023). Interhemispheric asymmetry of the thermospheric neutral density response to the 7–9 September 2017 geomagnetic storms. *Geophysical Research Letters*, *50*, e2023GL103208. https://doi.org/10.1029/2023GL103208

Received 9 FEB 2023
Accepted 19 MAY 2023

Interhemispheric Asymmetry of the Thermospheric Neutral Density Response to the 7–9 September 2017 Geomagnetic Storms

Qingyu Zhu[1], Gang Lu[1], Jiuhou Lei[2], Yue Deng[3], Eelco Doornbos[4], Jose van den IJssel[5], and Christian Siemes[5]

[1]High Altitude Observatory, National Center for Atmospheric Research, Boulder, CO, USA, [2]University of Science and Technology of China, Hefei, China, [3]University of Texas at Arlington, Arlington, TX, USA, [4]Royal Netherlands Meteorological Institute, De Bilt, The Netherlands, [5]Faculty of Aerospace Engineering, Delft University of Technology, Delft, The Netherlands

Abstract The thermospheric neutral density response to the 7–9 September 2017 storms is investigated based on the Swarm satellite observations and the thermosphere-ionosphere-electrodynamic general circulation model (TIEGCM) simulation. The Swarm data depicted a prominent interhemispheric asymmetry (IHA) in the afternoon sector during the second storm, a feature that was yet explained. Driven by realistic high-latitude electric potential and electron precipitation patterns, the TIEGCM is able to reproduce the observed storm-time neutral density response. The TIEGCM simulation reveals that the differences in the traveling atmospheric disturbances (TADs) is largely responsible for the observed IHA in the neutral mass density response at low and middle latitudes, whereas the difference in mean molecular mass between the two hemispheres may contribute to the IHA in neutral density at higher latitudes. The IHAs in TADs and mean molecular mass are attributed to the IHA in Joule heating dissipation on the night and dawn sides.

Plain Language Summary During geomagnetic storms, thermospheric neutral density can increase drastically due to intense heat inputs. Enhanced neutral density increases the air drag on satellites which could lower their orbits and lead to faster atmosphere reentering of satellites. In addition, enhanced neutral mass density may cause larger uncertainties in orbit prediction which increases the risk of collisions with other space objects. Therefore, it is essential to improve the understanding of storm-time neutral density variations to improve satellite operations. Recent satellite observations have revealed that thermospheric neutral mass density response can be interhemispherically asymmetric even under equinox conditions when the background density in the two hemispheres is comparable. This paper presents a case study of such an event based on data analysis and numerical simulations to investigate the physical mechanisms behind this intriguing phenomenon. The event took place on 7–9 September 2017 and the most prominent interhemispheric asymmetry of neutral density occurred in the afternoon sector. Our study found that the interhemispheric asymmetry during this event results from the differences in the generation, propagation and interaction of globally propagating atmospheric waves, namely traveling atmospheric disturbances, as well as the difference in mean molecular mass between the northern and southern hemispheres.

1. Introduction

During geomagnetic storms, a tremendous amount of electromagnetic energy is deposited in the Earth's thermosphere, which is mainly converted to Joule heating (Richmond, 2021) and significantly enhances thermospheric neutral density (Dang et al., 2022; Fang et al., 2022; Lin et al., 2022; Prölss, 2011; Zhu, Deng, et al., 2022). Enhanced neutral density exerts additional air drag on low Earth orbit (LEO) satellites flying in the thermosphere, which may lower satellites' orbit and cause the loss of satellite due to reentering into the Earth's atmosphere. In addition, enhanced neutral mass density may cause larger uncertainties in orbit prediction and increase the risk of collisions with other space objects (e.g., Oliveira & Zesta, 2019). Hence, a comprehensive understanding of the storm-time thermospheric neutral density response is crucial to satellite orbit determination and collision avoidance.

While thermospheric density undergoes an overall enhancement during geomagnetic storms, the enhancement can be asymmetric between the northern and southern hemispheres at some local times as revealed by satellite

measurements (e.g., Bruinsma et al., 2006; Ercha et al., 2012; Li & Lei, 2021; Sutton et al., 2005, 2009). For example, Li and Lei (2021) analyzed neutral density measurements from the Swarm-B satellite (~510 km) during the 7–9 September 2017 geomagnetic storm and found that the neutral mass density in the afternoon sector (~15.7 local time) experienced a significantly larger enhancement in the southern hemisphere (SH) than the northern hemisphere (NH), even though the event occurred near equinox when the background neutral density was expected to be symmetric between the two hemispheres. The cause of such an interhemispheric asymmetry in storm-time neutral density changes, however, was not elucidated in their work, which has motivated us to conduct further analysis of the event with numerical simulations.

As discussed in Lu et al. (2016), Joule heating can alter the local or global neutral mass density through three different pathways: First, enhanced Joule heating increases the neutral temperature, which causes the thermosphere to expand barometrically and increases the neutral density above the heating source (Rishbeth et al., 1969). Second, enhanced Joule heating induces an upwelling and increases the mean molecular mass at higher altitudes (Fuller-Rowell et al., 1997). Since the neutral scale height is proportional to the ratio of the neutral temperature to mean molecular mass, increased mean molecular mass can then offset the effect of increased neutral temperature on the scale height, and thus suppress the neutral density enhancement associated with increased temperature (Lei et al., 2010; Liu et al., 2014). Third, impulsive Joule heating dissipation triggers large-scale traveling atmospheric disturbances (TADs) which propagate globally and can modulate thermospheric properties everywhere (Richmond & Matsushita, 1975). Since Joule heating can be significantly asymmetric between the two hemispheres during geomagnetic storms (Knipp et al., 2021; Pakhotin et al., 2021), Li and Lei (2021) speculated that the stronger neutral density enhancement in the SH during the 7–9 September 2017 geomagnetic storms may result from a stronger Joule heating dissipation in the SH afternoon sector. However, no direct evidence has been provided to support such speculation. In addition, TADs initiated in one hemisphere can propagate into the opposite hemisphere and contribute to the neutral density variations therein (e.g., Bruinsma & Forbes, 2007; Guo et al., 2014; Zhu, Lu, & Deng, 2022). As a result, stronger neutral density enhancements in a given hemisphere may not necessarily require stronger Joule heating dissipated in that hemisphere.

In this study, we utilized the National Center for Atmospheric Research Thermosphere-Ionosphere-Electrodynamics General Circulation Model (NCAR-TIEGCM, Qian et al., 2014; Richmond et al., 1992) v2.0 to elucidate the physical processes responsible for the observed interhemispheric asymmetry in the storm-time neutral density enhancement during the 7–9 September 2017 geomagnetic storms. Details of the TIEGCM along with the neutral density data are described in Section 2. Section 3 presents the data-model comparisons as well as a detailed analysis of the simulation results. Section 4 summarizes the main findings of this study.

2. Data and Model

2.1. Neutral Mass Density Data

The Swarm mission consists of three satellites flying in near circular orbits. Swarm-A and Swarm-C fly side by side at an altitude of ~450 km with an inclination angle of 87.5°, and Swarm-B flies at an altitude of ~510 km with an inclination angle of 88°. During the 7–9 September 2017 geomagnetic storms, the ascending and descending nodes for Swarm-A/C were at ~10.2 LT and ~22.2 LT, respectively, while they were at ~15.7 LT and ~3.7 LT, respectively, for Swarm-B. For this event, only the neutral density data derived from the onboard Global Position System (GPS) receiver are available. Details about the GPS-based data can be found in van den IJssel et al. (2020). In addition, we use only the GPS-based neutral density data from Swarm-A and Swarm-B since the neutral density data from Swarm-C are very similar to that from Swarm-A.

2.2. TIEGCM

The TIEGCM is a global model of the ionosphere-thermosphere (I-T) system with self-consistent dynamic and electrodynamic processes (Qian et al., 2014; Richmond et al., 1992). This study uses the default version of the TIEGCM, which has a horizontal resolution of 2.5° in both geographic longitude and latitude and one-fourth scale height in altitude. The lower boundary is about 97 km and the top boundary ranges from 500 to 700 km depending on the solar and geomagnetic activity. The model is run at a time step of 5s and the model outputs are saved at a cadence of 5 min. The version of the TIEGCM used in this study treats helium as a major species and more details can be found in Sutton et al. (2015).

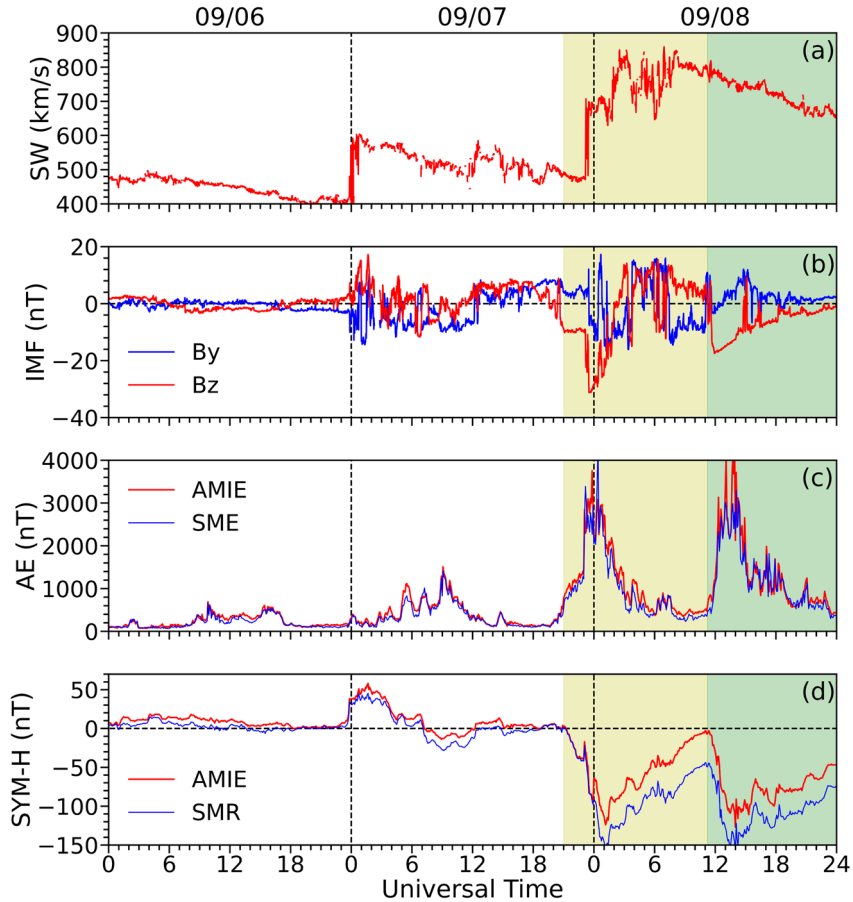

Figure 1. Evolutions of the (a) solar wind speed, (b) IMF B_y (Blue) and B_z (Red) components, (c) AE, (d) SYM-H between 09/06/2017 and 09/09/2017. The SuperMAG SME and SMR indices are shown in blue lines in panels (c) and (d), respectively, for comparisons.

In order to better specify high-latitude Joule heating in the TIEGCM, the electric potential and electron precipitation patterns derived from the Assimilative Mapping of Ionospheric Electrodynamics AMIE procedure (Richmond, 1992; Richmond & Kamide, 1988) are used to drive the TIEGCM. The data inputs to AMIE for this event include horizontal magnetic perturbations measured by 254 ground stations (among them 201 were in the NH and 53 in the SH), the line-of-sight ion drifts measured by the Super Dual Auroral Radar Network (SuperDARN) high-frequency radar network, the cross-track ion drift data measured by four Defense Meteorological Satellite Program (DMSP) satellites (i.e., F15, F16, F17 and F18), the electron precipitation data inferred from the Special Sensor of Ultraviolet Spectrographic Imager (SSUSI) onboard the DMSP F17 and F18 satellites, the horizontal magnetic perturbations measured by the Iridium satellite constellation and provided by the Active Magnetosphere and Planetary Electrodynamics Response Experiment (AMPERE) data set (Anderson et al., 2014), and the horizontal magnetic perturbations measured by the Swarm satellites. The temporal resolution of the AMIE pattern is 5 min, with a spatial resolution of 0.67 hr in magnetic local time (MLT) and 1.67° in magnetic latitude (MLAT). The AMIE patterns are spatiotemporally interpolated to the TIEGCM grids and model running time during the simulation.

3. Results and Discussions

Figure 1 exhibits the temporal evolutions of the solar wind speed, the interplanetary magnetic field (IMF) *y* and *z* components, the AE and SYM-H during 6–9 September 2017. The red lines in Figures 1c and 1d represent AMIE-derived AE and SYM-H which are calculated from the magnetometer data from 124 stations between |55°| and |76°| MLAT in both hemispheres and 56 stations between −40° and 40° MLAT, respectively, and both have

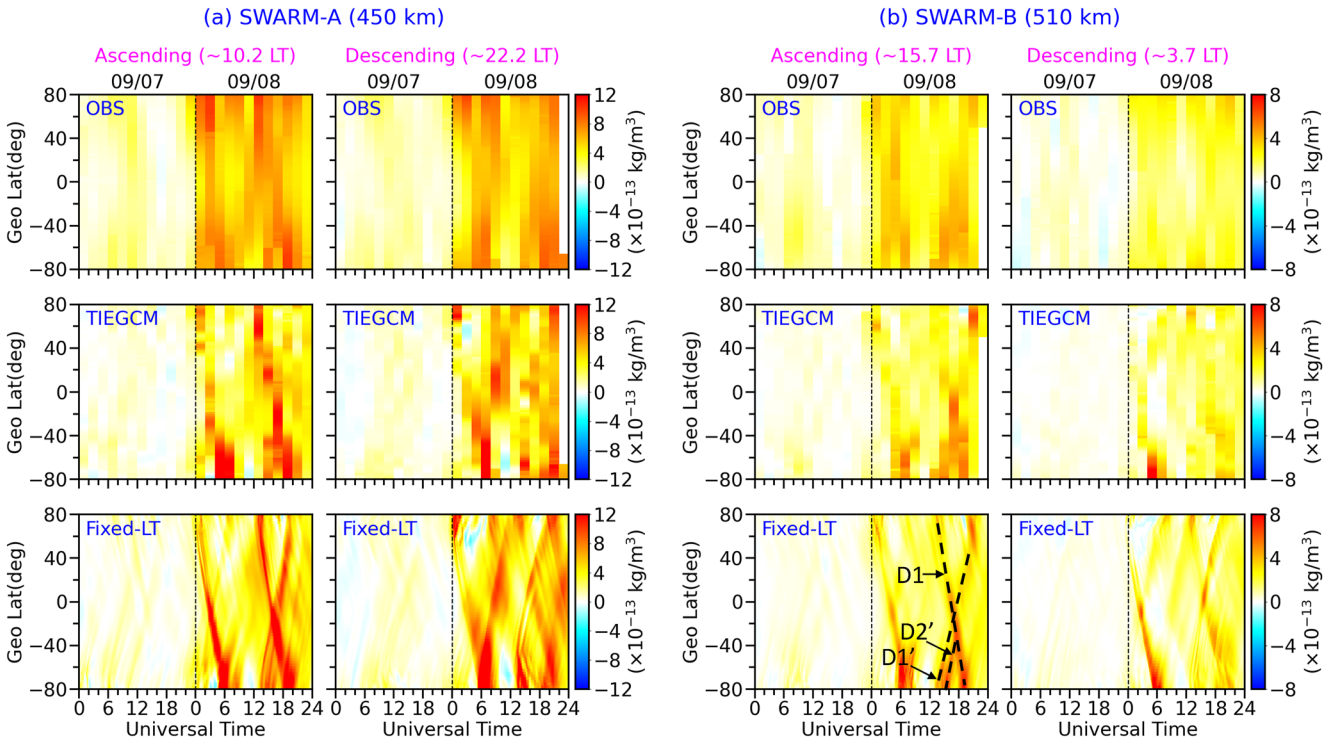

Figure 2. Storm-quiet differences of the neutral mass density ($\Delta\rho$) from the observation and simulation. For each column, the top and middle rows represent $\Delta\rho$ along the satellite trajectory from the observation and TIEGCM, respectively, and the bottom row represents $\Delta\rho$ from the TIEGCM at the fixed local time labeled at the top of each column. The black dashed lines in the bottom panel of the third column indicate the TADs.

a temporal resolution of 1 min. As a comparison, the equivalents of AE and SYM-H provided by SuperMAG, SME and SMR (Gjerloev, 2012; Newell & Gjerloev, 2011, 2012), are shown as blue lines in Figures 1c and 1d, and they are generally comparable with the AMIE AE and SYM-H indices. The 7–9 September 2017 storms were triggered by the interplanetary coronal mass ejections (ICMEs) and consisted of two storms as indicated by the SYM-H index (highlighted by the yellow and green shaded areas in Figure 1). During both storms, the AE index exceeded 3,000 nT and the SYM-H index dropped to about −120 nT.

Figure 2 presents the storm-quiet differences of the neutral mass density ($\Delta\rho$) at four LTs as a function of universal time (UT) and geographic latitude, and the neutral mass density on 09/06 is used as the quiet-time reference. The LTs shown in Figures 2a and 2b correspond to those of the ascending and descending nodes of Swarm-A and Swarm-B satellites. For each column (i.e., each LT meridional plane), the top and middle rows show the $\Delta\rho$ determined from the measured and modeled neutral densities along the satellite trajectory, respectively. Note that the neutral density at the satellite trajectory height has been normalized to a constant height (i.e., 450 km for Swarm-A and 510 km for Swarm-B) based on the NRLMSISE-00 model (Picone et al., 2002) before calculating $\Delta\rho$ and details about the normalization can be found in Bruinsma et al. (2006). As shown in the Swarm observations (first row), $\Delta\rho$ in the NH is generally comparable with that in the SH at the LTs where the observations are available except at 15.7 LT. The $\Delta\rho$ value in the SH is larger than that in the NH during the second storm at 15.7 LT while the $\Delta\rho$ is comparable between the two hemispheres before the second storm. For the TIEGCM simulation results (second row), although some quantitative differences between model and data do exist, they are in good agreement with the Swarm measurements. In particular, the interhemispheric asymmetry in the neutral density enhancement observed by Swarm-B during the second storm at 15.7 LT is well captured by the TIEGCM. The plausible causes of this interhemispherically asymmetric behavior will be discussed later. Figure S1 in Supporting Information S1 shows the data-model comparison for the GRACE satellite which flies at ~350 km and has similar ascending and descending LTs as Swarm-A during this event (Yuan et al., 2019), and details about the GRACE density data used in this study are provided by March et al. (2021). Again, the data-model comparison shows a reasonable agreement. No significant interhemispheric asymmetry is shown in $\Delta\rho$ along the GRACE satellite path, which is consistent with the results for the Swarm-A satellite (Figure 2a).

The third row of Figure 2 shows the UT-latitude distribution of the simulated $\Delta\rho$ at a constant altitude (450 km for Swarm-A and 510 km for Swarm-B) using the 5-min model outputs at all latitudes for the four fixed LTs. Clearly, TADs are more discernible from $\Delta\rho$ in the bottom row than in the top two rows which are referred to as $\Delta\rho$-TADs hereafter. At 15.7 LT and during the second storm, there are several $\Delta\rho$-TADs originated in the polar regions of both hemispheres and propagating to lower latitudes or even into the opposite hemispheres. More specifically, a $\Delta\rho$-TAD is induced in the NH around 13 UT (marked as D1) and propagates toward lower latitudes at a phase speed of ~800 m/s. D1 then propagates into the SH and arrives at the SH polar region around 19 UT. In the SH, there are at least two $\Delta\rho$-TADs launched in the polar region around 14 and 15 UT (marked as D1′ and D2′), respectively, and they travel at a similar phase speed as the D1. Since D1′ and D2′ are induced later than D1, D1 interacts with D1′ and D2′ around 20°–40°S. The amplitudes of D1′ and D2′ are severely attenuated after interacting with D1.

Figure 3 displays the evolution of the simulated $\Delta\rho$-TADs at a fixed altitude of 450 km during the second storm from a polar view. D1, D1′, and D2′ labeled in Figure 2b are also marked in Figure 3. Besides D1′ and D2′, there is also a trans-polar propagating $\Delta\rho$-TAD (marked as D3′) in the SH, which is invisible in Figure 2 but contributes to the neutral density enhancement in the afternoon sector. D3 initiates around 60°S in the pre-midnight sector at 14:05 UT and propagates over the SH polar cap and drifts toward the afternoon sector due to the Coriolis force (Balthazor & Moffett, 1999). By 16:45 UT, the amplitude of D3′ is significantly attenuated. Figure 3 shows that D1′, D2′, and D3′ lead to significant neutral density enhancements at middle and high latitudes in the SH at 15.7 LT (black radial line) between 14:45 UT and 16:45 UT. However, no significant neutral mass density enhancement occurs at middle and high latitudes in the NH at 15.7 LT during this period. Consequently, there is a significant interhemispheric asymmetry in neutral mass density enhancement at middle and high latitudes and near 15.7 LT between 14:45 UT and 16:45 UT.

In the afternoon sector, since D1 arrives at the equator earlier than D1′, D1 and D1′ interact in the SH between 16:05 and 16:45 UT. D1 continues propagating into the SH and interferes with D2′ later on. The interaction between D1 and D2′ results in the neutral mass density enhancements in a broad latitudinal range in the SH in the afternoon sector. After that, D1 arrives in the SH polar region at 18:05 UT whereas D1′ remains around the geographic equator in the afternoon sector. As a result, the neutral density in the SH undergoes a large enhancement from the equator to the polar region at 15.7 LT between 16:45 UT and 18:05 UT while the NH neutral density does not. After 18:05 UT, D1′ starts contributing to the neutral mass density enhancement in the NH and in the afternoon sector but its amplitude is attenuated as it propagates northward to higher latitudes. Consequently, the neutral density enhancement in the NH is generally smaller than that in the SH at 15.7 LT between 18:05 UT and 20:05 UT. The interactions between $\Delta\rho$-TADs can also be seen in Figure S2 in Supporting Information S1.

Figure 4 shows $\Delta\rho$ along with the storm-quiet differences of the meridional wind (ΔV_n), mean molecular mass (Δm) and neutral temperature (ΔT_n) at 450 km and 15.7 LT as a function of UT and geographic latitude. Movie S1 displays the temporal evolutions of $\Delta\rho$, ΔN, ΔV_n, Δm, and ΔT_n at 450 km from a polar view. TADs can also be seen clearly in ΔN, ΔV_n, and ΔT_n, which are similar to those in $\Delta\rho$ in terms of phase propagation. Particularly, ΔN displays similar interhemispherically asymmetric response as $\Delta\rho$, i.e., a stronger response in the SH than the NH (Figure 4b). Changes in Δm, on the other hand, are largely confined to the region above |50°| GLAT, with a larger increase in the NH than the SH (Figure 4d). Larger enhancements of mean molecular mass in the NH can effectively offset the enhancements of neutral scale height caused by increased neutral temperature, and thus suppress increases of number density (Lei et al., 2010; Liu et al., 2014). Consequently, even though TADs can cause strong enhancements of T_n above 50°N GLAT (Figure 4e), changes in ρ and N are less evident than those in the SH for comparable ΔT_n (Figures 4a and 4b).

The interhemispheric asymmetry of TADs is related to the interhemispheric asymmetry in Joule heating dissipations between the two hemispheres as shown in Figure 5. The generations of D1 in the NH and D1′–D3' in the SH stem from the enhanced Joule heating dissipation between 12:45 UT and 14:05 UT, which mainly occur on the dawn side in the NH and on the night side in the SH, respectively. In other words, there is no strong Joule heating deposited in the afternoon sector during the second storm where strong neutral density enhancements are observed. Therefore, the TADs seen at a given local time and at middle and low latitudes do not necessarily mean that there is a concurrent high-latitude heating source at that local time, which is consistent with Lu et al. (2016). Figure S3 in Supporting Information S1 compares Joule heating dissipations in the different hemispheres during the first storm. Again, Joule heating is mostly dissipated on the night and dawn sides. Moreover, Joule heating

10.1029/2023GL103208

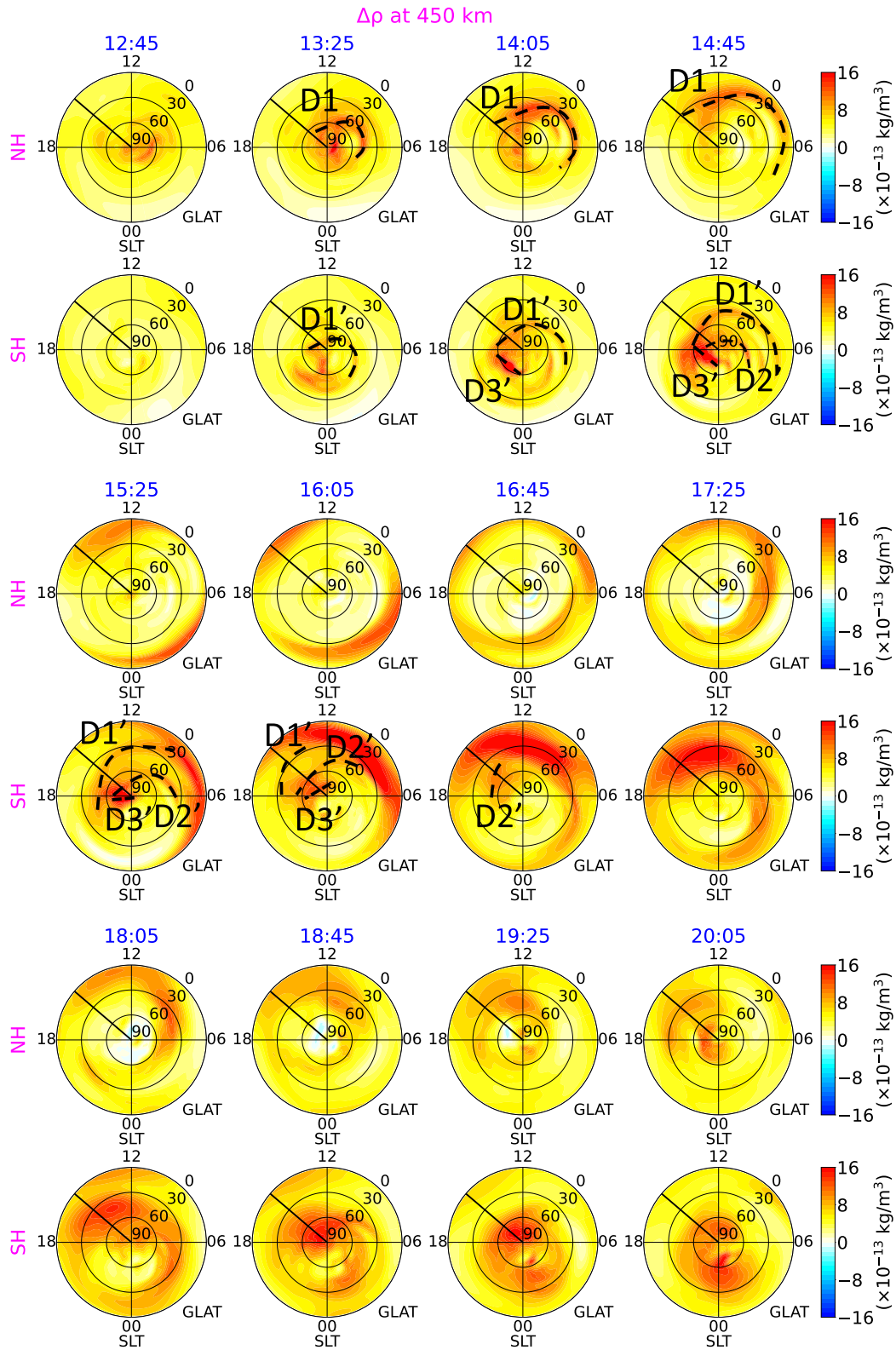

Figure 3. Storm-quiet difference of the neutral mass density ($\Delta\rho$) at 450 km at different UTs on 09/08/2017 from the TIEGCM simulation. The first, third and fifth rows are NH results while other rows are the SH results. All subplots are present in geographic coordinates and in polar views. The 15.7 LT is marked by the black radial line in each plot and the black dashed lines indicate the $\Delta\rho$-TADs.

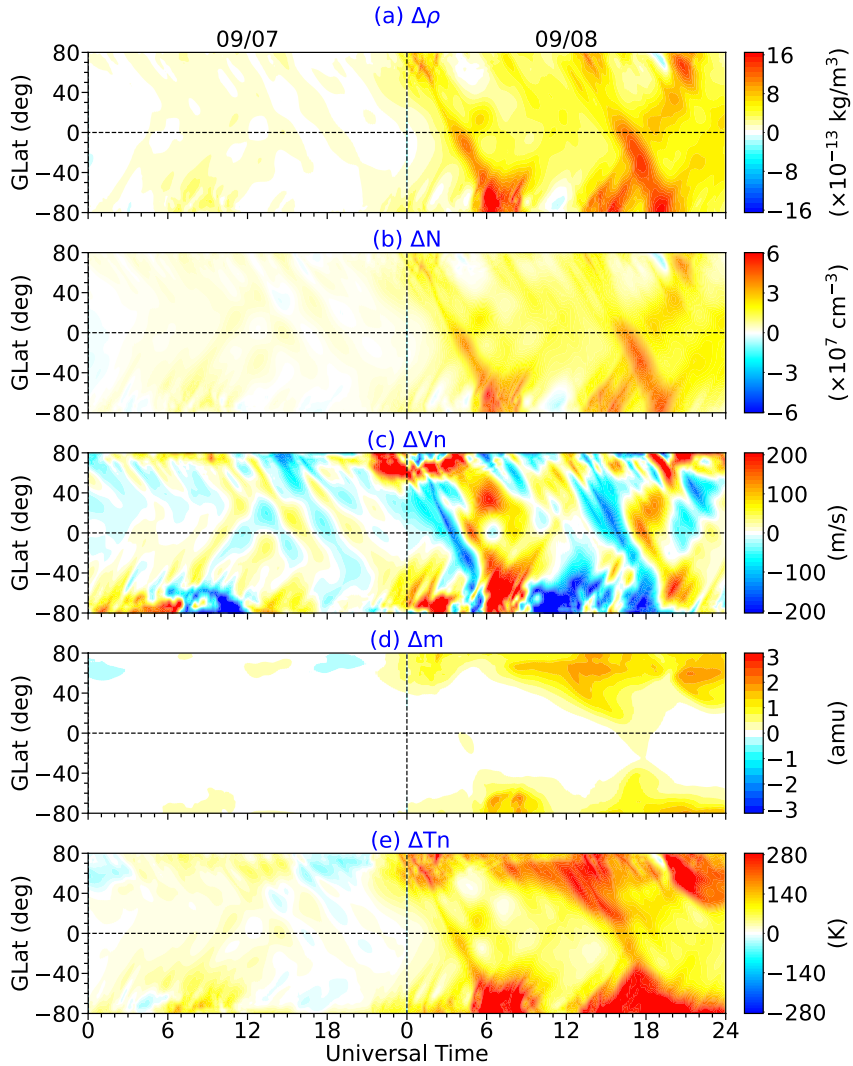

Figure 4. Evolutions of storm-quiet differences of (from top to bottom) the neutral mass density ($\Delta\rho$), neutral number density (ΔN), meridional wind (ΔV_n), mean molecular mass (Δm) and neutral temperature (ΔT_n) at 450 km and at LT = 15.7 from TIEGCM outputs. For the meridional wind, positive values indicate northward winds.

dissipated on the dawn side is much stronger in the NH than that in the SH, causing stronger and more equatorward composition perturbations in the NH on the dawn side (Movie S1). The perturbed composition then corotates with the Earth into afternoon (Cai et al., 2023) and contributes to the interhemispheric asymmetry in the afternoon neutral density response.

4. Summary

In this study, the thermospheric neutral density response to the 7–9 September 2017 storms is studied based on a combination of data analysis and the TIEGCM simulation using the electric potential and electron precipitation patterns derived from the AMIE procedure. It is found that the TIEGCM can well capture the storm-time thermospheric neutral density response observed by the Swarm satellites. In particular, the interhemispheric asymmetry of the neutral density response observed by the Swarm-B satellite in the afternoon sector during the second storm is well reproduced in the TIEGCM simulation. It is found that the difference in the TADs between the northern and southern hemispheres is mainly responsible for the interhemispheric asymmetry in the mid- and low-latitude regions, whereas the difference in mean molecular mass may contribute to the interhemispheric asymmetry at higher latitudes. This study unveils how Joule heating can contribute to the observed interhemispheric asymmetry

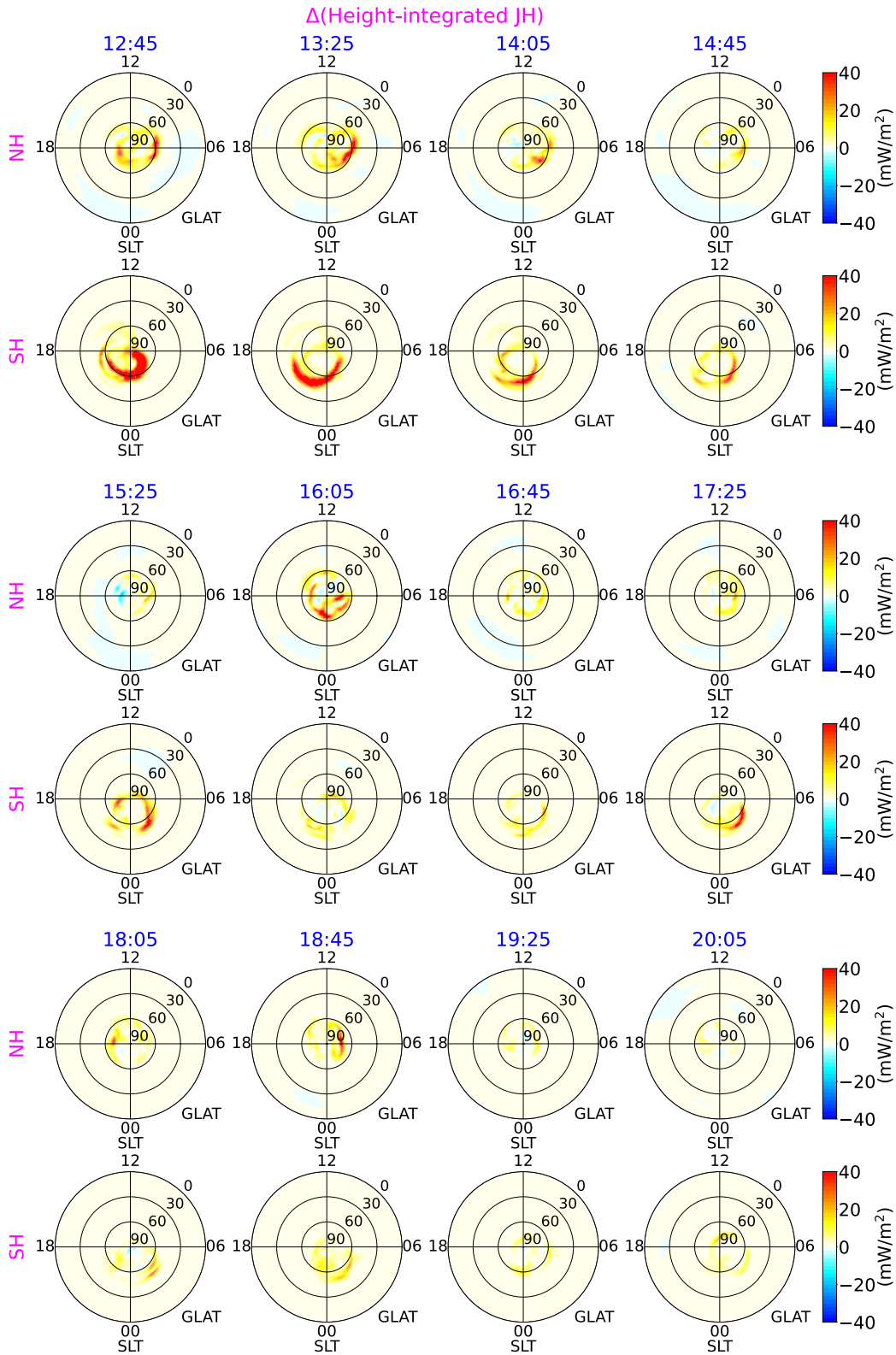

Figure 5. Same as Figure 3 except for storm-quiet difference of height-integrated Joule heating.

in the neutral density response to the 7–9 September 2017 storms. In future studies, we plan to explore how the lower-atmospheric forcings (e.g., Stober et al., 2021) may affect the interhemispheric asymmetry of thermospheric density variations.

Data Availability Statement

The IMF, solar wind data can be found at https://omniweb.gsfc.nasa.gov. The SME and SMR data can be found at https://supermag.jhuapl.edu. The Swarm neutral density data can be found at https://swarm-diss.eo.esa.int/#swarm%2FLevel2daily%2FEntire_mission_data%2FDNS%2FPOD and the GRACE neutral density data can be found at https://swarm-diss.eo.esa.int/#swarm%2FMultimission%2FGRACE%2FDNS%2FSat_1. The TIEGCM simulation outputs and data used in this study are stored at: https://doi.org/10.5065/8yvd-fs62.

Acknowledgments
QZ was supported by the NCAR ASP Postdoctoral Fellowship. GL was supported by NASA Grants 80NSSC17K071 and 80NSSC21K1673. QZ and GL were also supported by the NASA Grant 80NSSC22K0061 through the subaward 2021GC1619. YD was supported by AFOSR award FA9559-16-1-0364 and NASA Grants 80NSSC20K0195 and 80NSSC20K0606. This material is based upon work supported by the National Center for Atmospheric Research, which is a major facility sponsored by the National Science Foundation under Cooperative Agreement No. 1852977. This research was supported by the International Space Science Institute (ISSI) in Bern and Beijing, through ISSI International Team project #511 (Multi-Scale Magnetosphere-Ionosphere-Thermosphere Interaction). We would like to acknowledge high-performance computing support from Cheyenne (https://doi.org/10.5065/D6RX99HX) provided by National Center for Atmospheric Research's Computational and Information Systems Laboratory, sponsored by the National Science Foundation. We gratefully acknowledge the SuperMAG collaborators (http://supermag.jhuapl.edu/info/?page=acknowledgement). We also thank Wenbin Wang for his comments on the initial draft.

References

Anderson, B. J., Korth, H., Waters, C. L., Green, D. L., Merkin, V. G., Barnes, R. J., & Dyrud, L. P. (2014). Development of large-scale Birkeland currents determined from the active magnetosphere and planetary electrodynamics response experiment. *Geophysical Research Letters*, *41*(9), 3017–3025. https://doi.org/10.1002/2014GL059941

Balthazor, R. L., & Moffett, R. J. (1999). Morphology of large-scale traveling atmospheric disturbances in the polar thermosphere. *Journal of Geophysical Research*, *104*(A1), 15–24. https://doi.org/10.1029/1998JA900039

Bruinsma, S., Forbes, J. M., Nerem, R. S., & Zhang, X. (2006). Thermosphere density response to the 20–21 November 2003 solar and geomagnetic storm from CHAMP and GRACE accelerometer data. *Journal of Geophysical Research*, *111*(A6), A06303. https://doi.org/10.1029/2005JA011284

Bruinsma, S. L., & Forbes, J. M. (2007). Global observation of traveling atmospheric disturbances (TADs) in the thermosphere. *Geophysical Research Letters*, *34*(14), L14103. https://doi.org/10.1029/2007GL030243

Cai, X., Wang, W., Lin, D., Eastes, R. W., Qian, L., Zhu, Q., et al. (2023). Investigation of the southern hemisphere mid-high latitude thermospheric $\sum O/N_2$ responses to the Space-X storm. *Journal of Geophysical Research: Space Physics*, *128*(3), e2022JA031002. https://doi.org/10.1029/2022JA031002

Dang, T., Li, X., Luo, B., Li, R., Zhang, B., Pham, K., et al. (2022). Unveiling the space weather during the Starlink satellites destruction event on 4 February 2022. *Space Weather*, *20*(8), e2022SW003152. https://doi.org/10.1029/2022SW003152

Ercha, A., Ridley, A. J., Zhang, D., & Xiao, Z. (2012). Analyzing the hemispheric asymmetry in the thermospheric density response to geomagnetic storms. *Journal of Geophysical Research*, *117*(A8), 8317. https://doi.org/10.1029/2011JA017259

Fang, T.-W., Kubaryk, A., Goldstein, D., Li, Z., Fuller-Rowell, T., Millward, G., et al. (2022). Space weather environment during the SpaceX Starlink satellite loss in February 2022. *Space Weather*, *20*(11), e2022SW003193. https://doi.org/10.1029/2022SW003193

Fuller-Rowell, T. J., Codrescu, M. V., Roble, R. G., & Richmond, A. D. (1997). How does the thermosphere and ionosphere react to a geomagnetic storm? In B. T. Tsurutani, W. D. Gonzalez, Y. Kamide, & J. K. Arballo (Eds.), *Geophysical monograph series* (Vol. 98, pp. 203–225). American Geophysical Union. https://doi.org/10.1029/GM098p0203

Gjerloev, J. W. (2012). The SuperMAG data processing technique. *Journal of Geophysical Research*, *117*(A9), A09213. https://doi.org/10.1029/2012JA017683

Guo, J., Liu, H., Feng, X., Wan, W., Deng, Y., & Liu, C. (2014). Constructive interference of large-scale gravity waves excited by interplanetary shock on 29 October 2003: CHAMP observation. *Journal of Geophysical Research: Space Physics*, *119*(8), 6846–6851. https://doi.org/10.1002/2014JA020255

Knipp, D., Kilcommons, L., Hairston, M., & Coley, W. R. (2021). Hemispheric asymmetries in Poynting flux derived from DMSP spacecraft. *Geophysical Research Letters*, *48*(17), e2021GL094781. https://doi.org/10.1029/2021GL094781

Lei, J., Thayer, J. P., Burns, A. G., Lu, G., & Deng, Y. (2010). Wind and temperature effects on thermosphere mass density response to the November 2004 geomagnetic storm. *Journal of Geophysical Research*, *115*(A5), A05303. https://doi.org/10.1029/2009JA014754

Li, R., & Lei, J. (2021). Responses of thermospheric mass densities to the October 2016 and September 2017 geomagnetic storms revealed from multiple satellite observations. *Journal of Geophysical Research: Space Physics*, *126*(1), e2020JA028534. https://doi.org/10.1029/2020JA028534

Lin, D., Wang, W., Garcia-Sage, K., Yue, J., Merkin, V., McInerney, J. M., et al. (2022). Thermospheric neutral density variation during the "SpaceX" storm: Implications from physics-based whole geospace modeling. *Space Weather*, *20*(12), e2022SW003254. https://doi.org/10.1029/2022SW003254

Liu, X., Thayer, J. P., Burns, A., Wang, W., & Sutton, E. (2014). Altitude variations in the thermosphere mass density response to geomagnetic activity during the recent solar minimum. *Journal of Geophysical Research: Space Physics*, *119*(3), 2160–2177. https://doi.org/10.1002/2013JA019453

Lu, G., Richmond, A. D., Lühr, H., & Paxton, L. (2016). High-latitude energy input and its impact on the thermosphere. *Journal of Geophysical Research: Space Physics*, *121*(7), 7108–7124. https://doi.org/10.1002/2015JA022294

March, G., van den IJssel, J., Siemes, C., Visser, P. N. A. M., Doornbos, E. N., & Pilinski, M. (2021). Gas-surface interactions modelling influence on satellite aerodynamics and thermosphere mass density. *Journal of Space Weather and Space Climate*, *11*, 54. https://doi.org/10.1051/swsc/2021035

Newell, P. T., & Gjerloev, J. W. (2011). Evaluation of SuperMAG auroral electrojet indices as indicators of substorms and auroral power. *Journal of Geophysical Research*, *116*(A12), A12211. https://doi.org/10.1029/2011JA016779

Newell, P. T., & Gjerloev, J. W. (2012). SuperMAG-based partial ring current indices. *Journal of Geophysical Research*, *117*(A5), A05215. https://doi.org/10.1029/2012JA017586

Oliveira, D. M., & Zesta, E. (2019). Satellite orbital drag during magnetic storms. *Space Weather*, *17*(11), 1510–1533. https://doi.org/10.1029/2019SW002287

Pakhotin, I. P., Mann, I. R., Xie, K., Burchill, J. K., & Knudsen, D. J. (2021). Northern preference for terrestrial electromagnetic energy input from space weather. *Nature Communications*, *12*(1), 1. https://doi.org/10.1038/s41467-020-20450-3

Picone, J. M., Hedin, A. E., Drob, D. P., & Aikin, A. C. (2002). NRLMSISE-00 empirical model of the atmosphere: Statistical comparisons and scientific issues. *Journal of Geophysical Research*, *107*(A12), SIA15-1–SIA15-16. https://doi.org/10.1029/2002JA009430

Prölss, G. W. (2011). Density perturbations in the upper atmosphere caused by the dissipation of solar wind energy. *Surveys in Geophysics*, *32*(2), 101–195. https://doi.org/10.1007/s10712-010-9104-0

Qian, L., Burns, A. G., Emery, B. A., Foster, B., Lu, G., Maute, A., et al. (2014). The NCAR TIE-GCM: A community model of the coupled thermosphere/ionosphere system. In J. Huba, R. Schunk, & G. Khazanov (Eds.), *Geophysical monograph series* (pp. 73–83). John Wiley and Sons, Ltd. https://doi.org/10.1002/9781118704417.ch7

Richmond, A. D. (1992). Assimilative mapping of ionospheric electrodynamics. *Advances in Space Research*, *12*(6), 59–68. https://doi.org/10.1016/0273-1177(92)90040-5

Richmond, A. D. (2021). Joule heating in the thermosphere. In W. Wang, Y. Zhang, & L. J. Paxton (Eds.), *Geophysical monograph series* (1st ed., pp. 1–18). Wiley. https://doi.org/10.1002/9781119815631.ch1

Richmond, A. D., & Kamide, Y. (1988). Mapping electrodynamic features of the high-latitude ionosphere from localized observations: Technique. *Journal of Geophysical Research*, *93*(A6), 5741–5759. https://doi.org/10.1029/JA093iA06p05741

Richmond, A. D., & Matsushita, S. (1975). Thermospheric response to a magnetic substorm. *Journal of Geophysical Research*, *80*(19), 2839–2850. https://doi.org/10.1029/JA080i019p02839

Richmond, A. D., Ridley, E. C., & Roble, R. G. (1992). A thermosphere/ionosphere general circulation model with coupled electrodynamics. *Geophysical Research Letters*, *19*(6), 601–604. https://doi.org/10.1029/92GL00401

Rishbeth, H., Moffett, R. J., & Bailey, G. J. (1969). Continuity of air motion in the mid-latitude thermosphere. *Journal of Atmospheric and Terrestrial Physics*, *31*(8), 1035–1047. https://doi.org/10.1016/0021-9169(69)90103-2

Stober, G., Kuchar, A., Pokhotelov, D., Liu, H., Liu, H.-L., Schmidt, H., et al. (2021). Interhemispheric differences of mesosphere–lower thermosphere winds and tides investigated from three whole-atmosphere models and meteor radar observations. *Atmospheric Chemistry and Physics*, *21*(18), 13855–13902. https://doi.org/10.5194/acp-21-13855-2021

Sutton, E. K., Forbes, J. M., & Knipp, D. J. (2009). Rapid response of the thermosphere to variations in Joule heating. *Journal of Geophysical Research*, *114*(A4), A04319. https://doi.org/10.1029/2008JA013667

Sutton, E. K., Forbes, J. M., & Nerem, R. S. (2005). Global thermospheric neutral density and wind response to the severe 2003 geomagnetic storms from CHAMP accelerometer data. *Journal of Geophysical Research*, *110*(A9), A09S40. https://doi.org/10.1029/2004JA010985

Sutton, E. K., Thayer, J. P., Wang, W., Solomon, S. C., Liu, X., & Foster, B. T. (2015). A self-consistent model of helium in the thermosphere. *Journal of Geophysical Research: Space Physics*, *120*(8), 6884–6900. https://doi.org/10.1002/2015JA021223

van den IJssel, J., Doornbos, E., Iorfida, E., March, G., Siemes, C., & Montenbruck, O. (2020). Thermosphere densities derived from Swarm GPS observations. *Advances in Space Research*, *65*(7), 1758–1771. https://doi.org/10.1016/j.asr.2020.01.004

Yuan, L., Jin, S., & Calabia, A. (2019). Distinct thermospheric mass density variations following the September 2017 geomagnetic storm from GRACE and Swarm. *Journal of Atmospheric and Solar-Terrestrial Physics*, *184*, 30–36. https://doi.org/10.1016/j.jastp.2019.01.007

Zhu, Q., Deng, Y., Sheng, C., Anderson, P., & Bukowski, A. (2022). Impact of soft electron precipitation on the thermospheric neutral mass density during geomagnetic storms: GITM simulations. *Geophysical Research Letters*, *49*(11), e2021GL097260. https://doi.org/10.1029/2021GL097260

Zhu, Q., Lu, G., & Deng, Y. (2022). Low- and mid-latitude ionospheric response to the 2013 St. Patrick's Day geomagnetic storm in the American sector: Global ionosphere thermosphere model simulation. *Frontiers in Astronomy and Space Sciences*, *9*. https://doi.org/10.3389/fspas.2022.916739